AIAA JOURNAL
Vol. 40, No. 12, December 2002

Elliptic Instability of Counter-Rotating Vortices: Experiment and Direct Numerical Simulation

Florent Laporte*
European Center for Research and Advanced Training in Scientific Computation, F-31057 Toulouse Cedex 1, France
and
Thomas Leweke†
Institut de Recherche sur les Phénomènes Hors Equilibre, F-13384 Marseille Cedex 13, France

The short-wavelength elliptic instability of a pair of closely spaced counter-rotating vortices is analyzed using water tank experiments and direct numerical simulations. Qualitative and quantitative comparison shows excellent agreement and validates each of these complementary approaches. Both sets of results are used to give a detailed description of the instability characteristics. In the initial phase, the vortices are subject to a three-dimensional perturbation of their internal structure, with a wavelength scaling on the vortex core size and a distinct phase relationship between the two vortices. In the nonlinear evolution of the flow, the growth of the perturbations leads to the generation of secondary vortices and the breakdown of the initial pair into small-scale turbulence, accompanied by a rapid decrease of the average circulation. The growth rate of the instability is found to be higher than the one of the well-known Crow instability. The interaction between both mechanisms is also investigated, and an even faster decay of circulation is observed than for the cases where each instability acts alone. The relevance of these results for realistic aircraft trailing wakes is discussed.

Nomenclature

a	=	vortex core radius
a/b	=	initial dimensionless core size, $\equiv a_0/b_0$
b	=	vortex separation distance
d	=	diameter of invariant surface (tube)
E	=	initial kinetic energy
h	=	local direct numerical simulation grid spacing
k	=	wave number of the instability, $\equiv 2\pi/\lambda$
Re	=	Reynolds number, $\equiv \Gamma_0/\nu$
r	=	ratio E_{k_e}/E_{k_c}
$r_{\max}$	=	radius of maximum swirl velocity, $\approx 1.12a$
r, ϕ	=	radial and azimuthal coordinates of one vortex
t	=	time
v	=	velocity
x, y, z	=	horizontal, vertical, and axial coordinates
Γ	=	circulation of each vortex
λ	=	wavelength of the elliptic instability
ν	=	kinematic viscosity
σ	=	growth rate
ω	=	vorticity

Subscripts

c	=	related to the Crow[5] mode
e	=	related to the elliptic mode
h	=	related to the local mesh
k	=	related to the Fourier mode with wave number k
max	=	maximum
x, y, z	=	horizontal, vertical, axial
ϕ	=	azimuthal
0	=	initial

Superscripts

(linear)	=	related to the start of exponential growth
(onset)	=	related to the start of growth of the elliptic mode
S	=	related to invariant streamline tube
V	=	related to invariant vorticity tube
*	=	nondimensionalized using the time $2\pi b_0^2/\Gamma_0$

I. Introduction

THE dynamics of aircraft trailing wakes, whose large-scale structure consists mainly of two counter-rotating vortices, have been actively investigated since the early 1970s, when it became clear that the strong vortices behind heavy aircraft represent a potential hazard to others following behind due to the rolling moment and downwash they induce. This is particularly dangerous near the ground, and today wake vortex behavior is the principal factor determining the minimum separation distances for takeoff and landing, thus limiting airport capacities. With the increase of air traffic and the advent of new very large transport aircraft in the near future, the problem of understanding, predicting, and eventually controlling aircraft trailing wakes has received new interest in recent years and has triggered a surge of activity on both sides of the Atlantic, as witnessed in several recent reviews.[1–4]

The characteristics of wake vortices behind real aircraft depend on the weight and speed of the latter, as well as on the details of the wing geometry. Their dynamics, and especially their lifetime, are influenced by a number of factors, including the distribution of vorticity, axial flow and turbulence in the vortex cores, the ratio of core size to vortex spacing, the characteristics of the surrounding fluid (turbulence intensity, shear), and the proximity of the ground. The interaction of all of these ingredients lead to very diverse and complicated scenarios, and the understanding of all of the aspects involved in wake vortex decay is still far from complete.

A necessary step toward a better understanding and the final goal of controlling this complicated flow is an analysis of the physical mechanisms that are acting (or that are possible) in this situation. An important subset of these mechanisms, directly relevant to the decay of the wake, are three-dimensional instabilities of a vortex pair. The most effective way to study these phenomena is to consider simplified configurations that can be analyzed in great detail and that are also more readily accessible to a theoretical treatment. This is the strategy adopted in the present work. Once these fundamental phenomena are fully understood, their relevance and potential usefulness for the applied problem of aircraft wakes, where many

Received 20 April 2001; revision received 12 December 2001; accepted for publication 29 May 2002.

*Researcher, Computational Fluid Dynamics Department, 42 Avenue Gaspard Coriolis.
†Senior Researcher, French National Center for Scientific Research, 49 Rue Frédéric Joliot-Curie, B.P. 146.

different mechanisms act together, can be addressed with much more confidence in a subsequent step.

Crow[5] was the first to study the stability of two counter-rotating vortices. These were modeled by a pair of parallel line vortices of equal and opposite circulation, which is the simplest possible representation of an aircraft wake. He found that the pair was unstable to wavy perturbations of the vortex axes, which are symmetric with respect to the central plane of the pair and whose axial wavelengths are typically 5–10 times the initial vortex spacing. This long-wavelength three-dimensional instability has subsequently been observed in numerous laboratory experiments[6–10] and field studies,[11–13] and it is still considered one of the most promising means for the destruction of aircraft trailing wakes.

Crow's[5] analysis also identified two modes of short-wavelength instability (symmetric and antisymmetric), with wavelengths smaller than one vortex spacing. However, Widnall et al.[14] pointed out that these modes are spurious because the assumptions for Crow's[5] theory are no longer valid at these wavelengths. They proposed a different mode of short-wave instability, associated with a change of the internal structure of the vortex cores. For this purpose, a slightly more complicated model for the trailing wake had to be considered, consisting of two inviscid Rankine-type vortices, with (almost) circular cores of constant vorticity, both subject to an external strain due to the presence of the other vortex. Subsequent stability analyses[15–17] confirmed the existence of short-wave instability in such strained vortices with finite size cores.

The strain that each vortex induces at the location of the other one results in a flow with locally elliptic streamlines near the vortex centers. Theoretical studies[18–22] have shown that such elliptical flow in an unbound domain is three-dimensionally unstable. The mechanism of instability is the amplification of inertial waves in the frame of reference moving with the rotating flow, through a resonant interaction with the external strain. For the case of an elliptical flow of finite extent, as, for example, in a strained vortex core, the unstable perturbations are identical to the ones predicted by Widnall et al.[14] and others for Rankine vortices. The two sets of theoretical results can, indeed, be directly related to each other.[23,24] (See also the recent review on elliptical instability by Kerswell.[25])

The present paper deals with this elliptic instability in the case of a flow consisting of two laminar vortices that are initially parallel and uniform along their axes and that do not contain axial flow in their cores. The flow is studied experimentally and numerically, using the Navier–Stokes equations, which means that viscous effects are included and that the vortices have a smooth vorticity distribution. This configuration is a slightly more realistic representation of the core structure of aircraft trailing vortices than the inviscid Rankine vortex pair considered by Widnall et al.[14] Although still an oversimplification, it contains the major ingredients of the "real" flow, and it allows a precise and detailed analysis of the elliptic instability. The main differences with realistic aircraft wake vortex pairs concern the Reynolds number and the rescaled core size; their relevance will be discussed in detail near the end of the paper. Theoretical stability analyses relevant to this flow problem were carried out recently by Eloy and Le Dizès[26] for a single Lamb–Oseen vortex in an external strain and by Billant et al.[24] for a Lamb dipole.

The results presented here come from two separate studies described in more detail in Refs. 23 and 27. The experimental study by Leweke and Williamson[23] was the first to identify and characterize the elliptic instability in a counter-rotating vortex pair clearly, although some observations of similar phenomena were reported earlier,[28,29] but without detailed analysis. The more recent direct numerical simulation by Laporte and Corjon[27] allowed a more thorough quantitative treatment, as well as a clarification of the influence of the initial conditions on the later stages of the instability, in particular on its interaction with the long-wavelength Crow[5] instability. Other simulations[30] of a vortex pair had already captured some aspects of the elliptic instability, but the initial conditions were somewhat unrealistic, and comparisons with experiment and/or theory were limited.

In the following, we present a close comparison between the results from the experimental study[23] and the direct numerical simulation[27] of the elliptic instability of a vortex pair, including previously unpublished material. The laminar vortex pair is a rare example of a flow that is accessible to both methods, and the flow parameters in both studies were chosen to be very close. The purpose of this comparison is twofold: 1) to provide an additional mutual validation of these two complementary approaches and 2) to give a thorough description of an intrinsic feature of the vortex pair flow, that is, the short-wave instability of the vortex cores, whose clear observation is still fairly recent.

Section II defines the relevant parameters governing the vortex pair flow under consideration and gives details of the experimental and numerical methods. In Sec. III, the elliptic instability is presented, showing its onset, spatial structure, wavelength and growth rate, nonlinear late stage, and the subsequent breakdown of the flow. Section IV deals with the interaction between the short-wave instability and the long-wave Crow[5] instability, and the influence of initial conditions is discussed there. Comments on the relevance to real aircraft wakes are given in Sec. V, followed by a Summary in Sec. VI.

II. Technical Details

A. Vortex Pair Flow

We consider a pair of viscous laminar vortices of equal and opposite circulation that are initially straight, parallel, uniform along their axes, and without axial flow in their cores. The vortices translate through mutual induction in the direction perpendicular to their axes and to the line joining the two centers. Such a pair is characterized by the circulation Γ of each vortex and the separation b between the vortex centers. In addition, the internal structure can be described by a characteristic core size a, which is the radius of the tube around the vortex center containing most of the vorticity. Experimental velocity measurements (see Ref. 23 for details) have shown that the initial flow can be approximated remarkably well by a superposition of two Oseen (or Lamb–Oseen) vortices (see also Ref. 27 for the assessment of this initial condition), that is, axisymmetric two-dimensional vortices with a Gaussian vorticity distribution, for which the azimuthal velocity v_ϕ as function of the distance r from the vortex center is given by

$$v_\phi(r) = (\Gamma/2\pi r)\{1 - \exp[-(r^2/a^2)]\} \tag{1}$$

The characteristic length a is linked to the location $r_{\max}$ of maximum circumferential velocity by $r_{\max} \approx 1.12a$.

In the following, Cartesian coordinates x, y, and z are used, designating the (horizontal) direction of the line joining the two vortex centers, the (vertical) direction of displacement of the pair, and the axial direction, respectively. The nondimensional parameters governing the flow are the Reynolds number Re based on the initial vortex circulation, and the initial dimensionless core size a_0/b_0. Here, initial means immediately after the vortex formation in the experiments and at the end of the adaptation process in the numerical simulations. (See following sections.) For convenience, the subscript 0 will be dropped when designating the initial dimensionless core size ($a/b = a_0/b_0$). Time t is also an important parameter in this evolving flow. It is nondimensionalized by the time it takes a pair of idealized point vortices of the same circulation, moving with a self-induced velocity $\Gamma_0/2\pi b_0$, to travel one vortex separation b_0: $t^* = t \cdot \Gamma_0/2\pi b_0^2$.

B. Experimental Techniques

For the experimental study, the flow was investigated in a rectangular water container with glass walls, measuring $180 \times 45 \times 60$ cm^3. Horizontal vortex pairs were generated near the water surface using two anodized aluminum plates hinged to a common base, whose free edges were machined to an angle of 30 deg. They could be moved in a symmetric way by a computer-controlled step motor located outside the water and linked to the plates by a system of gears and joints. When the flaps were impulsively closed, a pair of starting vortices was created at the sharp edges, which then continued to move down toward the bottom of the tank. The vortices were typically separated by a distance of 2.5 cm, and their length was approximately 170 cm. This high aspect ratio of the vortex pair was necessary to limit the influence of end effects that spread rapidly into the central part of the flow.

The flow was visualized using fluorescent dye, which was painted on the inside of the plates close to the sharp edges before the introduction of the whole apparatus into the water. Illumination was achieved with the light from a 5-W argon laser. Images were recorded on standard video tape using a charge-coupled device (CCD) camera, or on 35-mm color film. Quantitative measurements of velocity fields were obtained by digital particle image velocimetry (DPIV). For this method, the flow was seeded with small plastic particles of diameter 70 μm and density 1.03 g/cm^{-3}, illuminated by a sheet of laser light of 3–5-mm thickness. The time that the slightly heavy particles needed to settle down was far longer than the time for the fluid motion to die out after stirring the tank, leaving a sufficient time interval for the measurements. Sequences of images (624×476 pixels gray scale) of the time-dependent flow were recorded on standard VHS video, again using a CCD camera. Fluid velocities were calculated from particle displacements obtained by two-step cross correlations (with window shifting) between successive half-frames of one image ($\frac{1}{60}$-s separation). The DPIV measurements showed that the initial velocity profiles of the vortices are very well represented by the one of a Lamb–Oseen vortex with a Gaussian vorticity distribution given by Eq. (1). The initial vortex pair characteristics were determined shortly after the end of the vortex formation, that is, the end of the plate motion. They were found by a least-squares fit of the measured velocity field to a superposition of two Gaussian vortices with Γ_0, b_0, and a_0 as adjustable parameters. The core size a increases in time due to the viscous diffusion of vorticity. However, this growth is relatively slow compared to the growth of the instabilities and was not considered further in the experimental study. Figures 1a and 1c show a visualization of the flow at this stage. The pair is perfectly uniform, and no noticeable three-dimensional perturbation can be detected.

In the experimental study, the Reynolds number varied in a range between 2.4×10^3 and 2.8×10^3. The initial core radius, after the end of the vortex formation, was typically close to one-fifth of the vortex spacing, $a/b \approx 0.2$.

Other measurements concerning the spatial structure and the growth rate of the instability were obtained from image analysis of flow visualizations recorded on video or photographic film. A more detailed description of the experimental setup and methods, especially the DPIV measurements, as well as an analysis of the measurement errors leading to the uncertainties given in the following sections, can be found in Ref. 23.

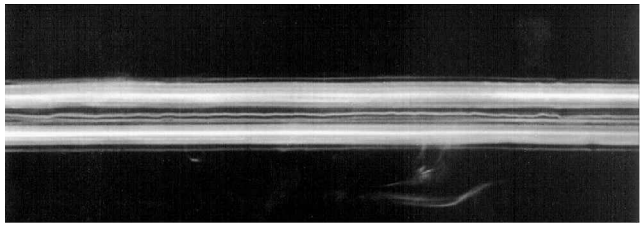

a) Experimental front view

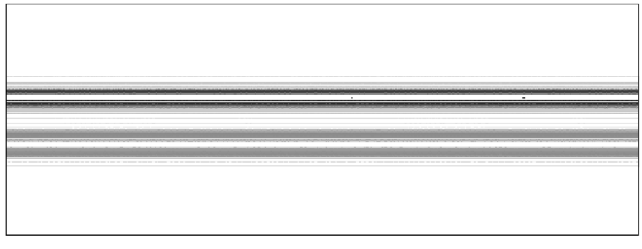

b) DNS front view

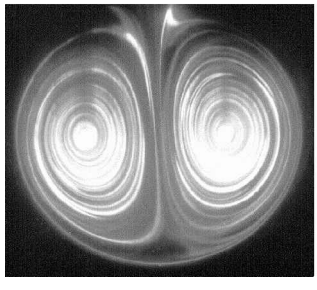

c) Experimental cross cut

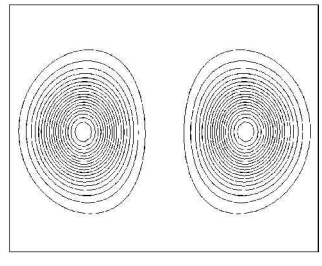

d) DNS cross cut

Fig. 1 Initial conditions: a) and c) experimental dye visualization for $Re = 2.75 \times 10^3$, $a/b = 0.2$, and $t^* = 1.7$; b) DNS contours of axial vorticity ω_z in an x–z plane and d) an x–y plane for $Re = 2.4 \times 10^3$, $a/b = 0.25$, and $t^* = 3.1$.

C. Numerical Method

The code used to perform the direct numerical simulations (DNS) of the vortex pair is a finite difference, parallel, three-dimensional, compressible Navier–Stokes solver (NTMIX3D), developed by the French Institute of Petroleum and the French Research Center on Turbulent Combustion. The temporal integration is achieved with a classical three-stage Runge–Kutta time-marching technique. A sixth-order compact scheme[31] was implemented for the discretization of the convective and viscous terms.

In the series of simulations presented here, the boundary conditions are periodic in the three directions, and the cross-sectional size of the simulation domain is chosen large enough (typically 4–5b_0) to keep the influence of the periodic vortex images at an acceptable level. As an illustration of the effect of these images, the modification of the descent speed of the pair, with respect to the case without images, can be estimated analytically to be about 8%, at first order. Larger dimensions than the ones used here have also been tested in both directions,[27] yielding very similar flow dynamics.

The discretization in the axial direction of the vortices uses between 8 and 36 grid points per wavelength of the elliptic instability, depending on the run. In the transverse directions, the discretization is such that there are 15 points inside the vortex core at the onset of the instability. The maximum local mesh Reynolds number $Re_h = (h_x|v_x| + h_y|v_y| + h_z|v_z|)/\nu$, based on the local mesh size and velocities, is found to be of the order of 40 before the onset of the instability, whereas it lies in the range 40–80 during the transition to turbulence, depending on the axial discretization used. Given that the Kolmogorov dissipation scale corresponds in principle to a local Reynolds number of order one, the present computations may be qualified as slightly underresolved.

The initial condition is obtained by the linear superposition of two Lamb–Oseen vortices [Eq. (1)]. The conditions are chosen to be close enough to the experimental values to allow meaningful comparisons. At the beginning of a run, the nondimensional core size is set to 0.179. Initially, each vortex adapts itself to the presence of the other one, in particular to the strain it experiences. (See Ref. 27 for details.) At the end of the adaptation period and at the beginning of the growth of the elliptic instability, the effective initial core size is found to be $a/b \approx 0.25$. The vorticity contours in Figs. 1b and 1d illustrate the flow structure at this stage. As for the experimental visualizations, the vortices have become slightly elliptic.

The Reynolds number is 2.4×10^3 in all runs. A white noise is added to the three Cartesian velocity components to trigger the instability. The amplitude of the noise is set to different values for different simulations, but is always lower than $5 \times 10^{-3} v_{\phi,\max}$, where $v_{\phi,\max}$ is the maximum circumferential velocity of one vortex. The different initial noise amplitudes basically only generate a temporal shift in the development of the elliptic instability in the corresponding simulations because different amounts of energy are initially fed into the elliptic mode. The results to be presented are extracted from different simulations without particular identification of the initial noise amplitude.

Throughout the paper, the results from experiments and numerical simulations will be shown in parallel, presented in a way that allows a close comparison of the two sets.

III. Elliptic Instability of a Vortex Pair

In this section, we focus exclusively on the elliptic instability during the different stages of its development. The interaction with the long-wavelength Crow[5] instability is treated in Sec. IV.

A. Onset and Initial Stages

The onset of the elliptic instability developing in any two-dimensional elliptical flow (i.e., a superposition of a solid-body rotation and a plane stagnation-point flow with uniform stretching) has been demonstrated to be due to a resonance between the neutral three-dimensional perturbation waves existing in such flows and the local strain experienced by the vortex.[15–22] The perturbation flow generated by the instability acts principally in the vicinity of the vortex core. The vortex centers are, therefore, efficient markers of the onset and initial stages of the instability. In particular, the displacement of the center with respect to its unperturbed position gives a measure of the instability amplitude and, subsequently, of its growth rate.

We begin with a qualitative description of the initial linear stage (with exponential growth) of the instability, through observations of the total perturbed flow. Figure 2 is a global view of the effect of the elliptic instability inside the vortex cores. In the experimental visualization, the vortex centers are marked by bright lines of dye. This line is observed to develop a wavy deformation, whose characteristic wavelength clearly scales on the vortex core size (Fig. 2a).

The detailed structure of the instability mode is visible in the close-up front views in Fig. 3. A cylindrical tube separates two regions of opposite radial motion in each vortex. The observed tube is composed of invariant streamlines (zero radial perturbation velocity) in the experiment, whereas it is an invariant tube of axial vorticity ω_z in the simulation. The existence of such invariant tubes has been demonstrated by Leweke and Williamson,[23] based on the work of Waleffe[21] on localized elliptic instability modes. The diameter of the invariant tube of axial vorticity is predicted[23] to be about 40% larger than the invariant streamline tube. This difference is visible in Fig. 3, and it is further confirmed by precise measurements (Sec. III.B). The two vortices also experience a remarkable in-phase axial variation of the elliptic mode. Leweke and Williamson[23] have shown that the observed phase relation is due to a matching condition linking the components of the velocity on both sides and normal to the median plane separating the vortices. The closer the vortices are (with respect to their core size), the stronger the continuity condition imposes itself on the flow.[24] As a consequence, for vortex pairs with significantly smaller ratios a/b (relevant to aircraft wake vortices), this condition may become too weak to override the initial phase selection by the noise exciting the unstable modes in each vortex. The phase relation is, therefore, expected to be random in such cases.

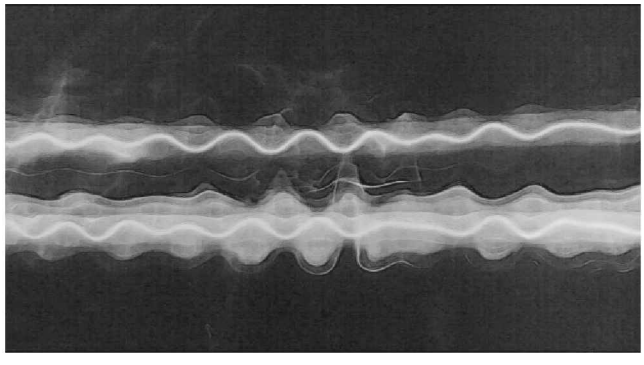

a) Experiment ($Re = 2.75 \times 10^3$, $a/b = 0.2$, and $t^* = 6.8$)

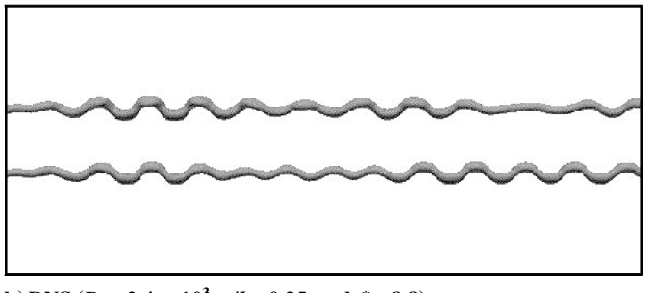

b) DNS ($Re = 2.4 \times 10^3$, $a/b = 0.25$, and $t^* = 8.8$)

Fig. 2 Global view of the elliptic instability mode in its linear regime.

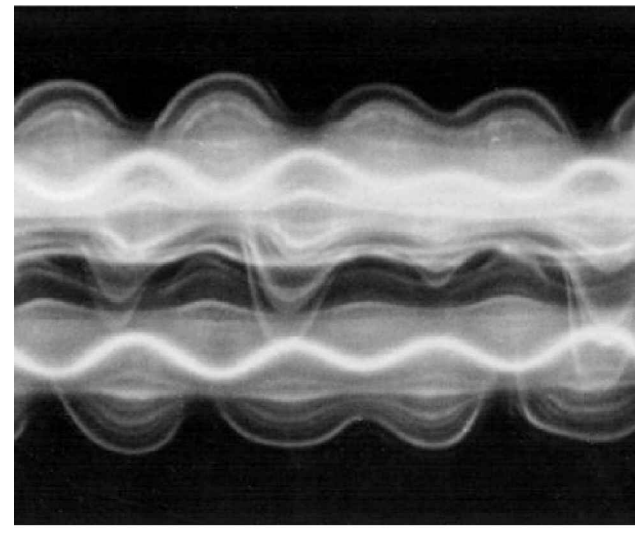

a) Experiment ($Re = 2.75 \times 10^3$, $a/b = 0.2$, and $t^* = 6.2$)

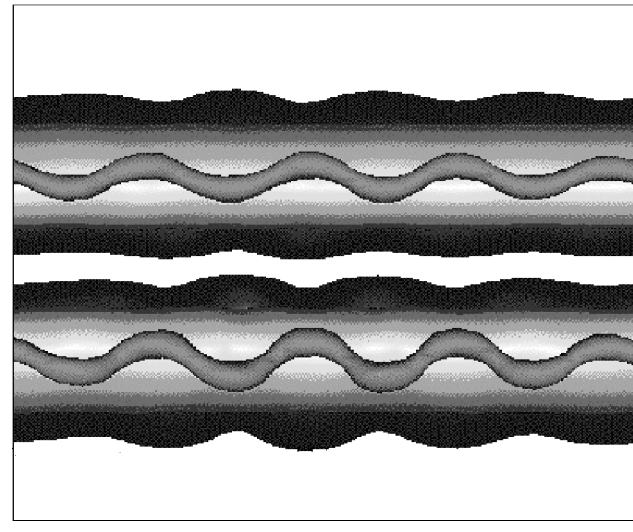

b) DNS ($Re = 2.4 \times 10^3$, $a/b = 0.25$, and $t^* = 10.8$)

Fig. 3 Detailed structure of the elliptic instability, which is found to be cooperative in the present flow with high a/b.

In the high-(a/b) flow considered here, the phase coupling is observed to occur strongly. The antisymmetric nature (in the sense of Crow[5]) of this coupling is well illustrated by the deformations of the vortex centerlines shown schematically in Fig. 4, where they are seen from three perpendicular directions. In the experiments, two simultaneous perpendicular visualizations similar to Fig. 3 were used to reconstruct the three-dimensional shape of the vortex centers, whereas in the simulations they were found by determining the local maxima of vorticity along the z axis. In the front views (Figs. 4a and 4d), the centers are displaced in phase, whereas in the side views (Figs. 4b and 4e), the deformations are out of phase. According to theoretical predictions,[18,19,21] the center of rotation of an elliptical flow should be shifted in the stretching direction of the local strain. In the present case, the strain in each vortex is induced by the presence of the other one, and the principal stretching axes are inclined about ± 45 deg with respect to the x axis, that is, the line joining the two initial vortex centers. The views along the z axis (Figs. 4c and 4f) show that the center deformations lie, indeed, in planes inclined by these angles and this independently of the phase coupling mentioned earlier.

To complement these observations made on the total flow, some characteristics of the perturbation itself are now presented. The axial vorticity ω_z of the elliptic perturbation mode can be deduced from the vorticity of the total flow shown in Figs. 5a and 5c. With the vorticity distribution of the (unperturbed) base flow of the vortex pair being antisymmetric with respect to the plane between the

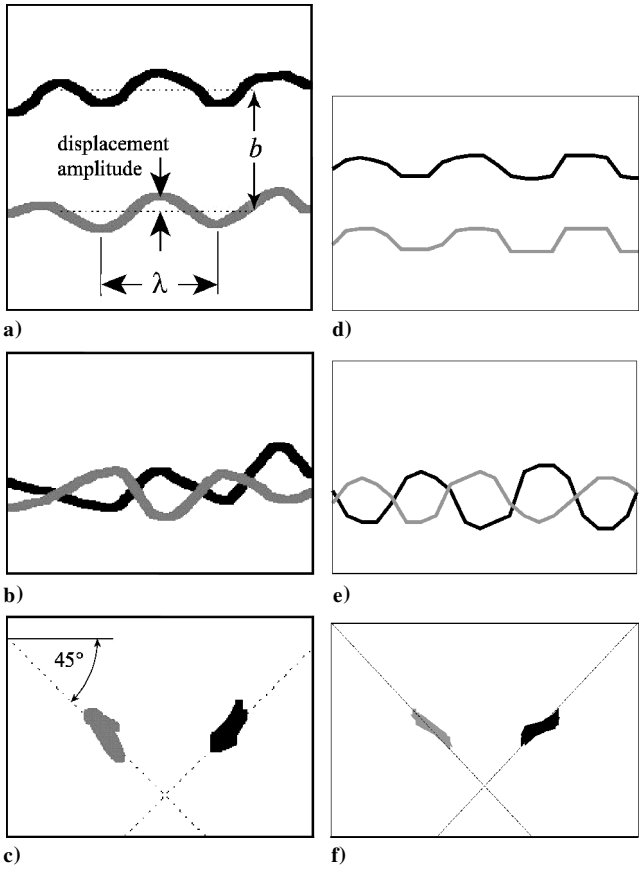

Fig. 4 Displacement of the vortex center lines seen from three perpendicular directions: a–c) experiment ($Re = 2.75 \times 10^3$, $a/b = 0.2$, and $t^* = 6.8$) and d–f) DNS ($Re = 2.75 \times 10^3$, $a/b = 0.2$, and $t^* = 6.8$).

vortices, and the perturbation being symmetric (despite the fact that the centerline deformations are antisymmetric; see Ref. 23), it is a simple matter to split the total flow into these two mutually exclusive parts. The resulting perturbation vorticity in Figs. 5b and 5d shows a characteristic two-lobe structure in each vortex, surrounded by a closed line of vanishing perturbation vorticity. This corresponds to the location of the invariant vorticity tubes in Fig. 3b. The patterns seen in Fig. 5 correspond to an axial location where the centerline deformation is maximal; they are, of course, modulated sinusoidally in the axial direction with the wavelength identifiable in Fig. 2. The particular shape of the axial vorticity perturbation mode is in good agreement with the one predicted theoretically[18,19,21] for localized modes of the elliptic instability under the assumption of small uniform external strain and also with the instability modes calculated for the case of a Lamb–Chaplygin vortex pair (see Refs. 24 and 30).

The azimuthal component of the perturbation vorticity ω_ϕ in each vortex is the same as the one of the total flow because the initial base flow possesses only axial vorticity. Figure 6 presents measurements of ω_ϕ in a y–z plane cutting through the center of one vortex. The distribution found in both experiment and calculation is composed of a three-row checkerboard pattern of opposite-signed vortical structures, which also closely matches theoretical predictions.[21,23]

B. Quantitative Results

In the experiments, quantitative measurements were obtained mainly from flow visualizations as in Figs. 2a and 3a. The shape of the vortex centerline deformation (see also Fig. 4a) directly gives the average wavelength of the instability, whereas its amplitude can be related to the amplitude of the elliptic instability mode,[23] whose evolution in time gives access to the instability growth rate. In the numerical study, these quantities were obtained from one-dimensional (axial) kinetic energy spectra, calculated using one-dimensional Fourier transforms. The wave number of the most amplified Fourier mode gives the axial wavelength and the variation of its amplitude the corresponding growth rate. (See Ref. 27 for details.) Incidentally, this procedure confirmed that the spatial resolution in the axial direction was sufficient because no energy accumulation was observed at the shortest simulated wavelengths.

1. *Wave Numbers*

According to theoretical results on elliptic instability in finite size domains, the axial instability wavelength λ scales on the cross-sectional extent of this region, that is, on the vortex core radius a in the present case. In the experiments, the nondimensional wave number ka of the elliptic instability, with $k = 2\pi/\lambda$ being the dimensional wave number, is found to be

$$ka = 1.6 \pm 0.2 \qquad \text{(experimental)} \tag{2}$$

using a value of a measured just after vortex formation. (Experimental error estimates are discussed in detail in Ref. 23.) The dimensional wave number k is measured during the linear regime of the instability. In the simulations, the wave number and the vortex radius have been measured a first time at the onset of the instability, that is, when the unstable Fourier mode first starts growing. The result is

$$ka^{(\text{onset})} = 1.87 \pm 0.15 \qquad \text{(numerical)} \tag{3}$$

which is reasonably close to the experimental value. The error estimates here and hereafter take into account the finite axial grid spacing used in the calculations and the uncertainty in determining the core size from the second moment of vorticity. The numbers in Eqs. (2) and (3) are quite different from the theoretical prediction of

$$ka = 2.26 \qquad \text{(theoretical)}^{26} \tag{4}$$

for an inviscid Gaussian vortex in a uniform external strain field. This is all the more significant because the most unstable wave numbers are expected to be located in a narrow band around this value. A second measurement was performed in the simulations once the exponential growth of the unstable mode had set in, for example, just after $t^* = 5$ in Fig. 7. By this time, the core size a had increased through viscous diffusion of vorticity, and the wave number was then found to be

$$ka^{(\text{linear})} = 2.35 \pm 0.19 \qquad \text{(numerical)} \tag{5}$$

which is now larger than the theoretical value.

Two observations must be taken into account when comparing our results with theory. First, the instability is triggered by either random background motion (experiment) or by a white noise (DNS). Both consist of a large number of modes that coexist initially and can lead, at a given wavelength, to transient behavior before the precise structure of the final unstable mode associated with this wavelength builds up. Second, because of the low Reynolds number and the relatively small viscous timescale, the base flow conditions evolve in time, which means that the mode (wavelength) observed in the end corresponds to some kind of optimal perturbation, that is, to a perturbation whose gain in amplitude is maximum over the selection period with changing conditions. This second issue was treated in detail in Ref. 26. These arguments suggest that, concerning the wave number selection, the comparison of the present results with those from inviscid stability theory, which considers a stationary base flow, should indeed be made at the time of mode selection, which lies somewhere between the times associated with the values in Eqs. (3) and (5). The mean value between them is $ka = 2.11$, which is in reasonable agreement with the theoretical value in Eq. (4).

Another possible source of discrepancies between experiment/simulation and theory may be that the latter considers almost circular vortices in a uniform external strain, whereas, in the vortex pair flow studied here, the strain induced by one vortex on the other is far from uniform, and each vortex is deformed elliptically. Although a precise analysis of these effects is lacking, note that the stability analysis in Ref. 24 of a Lamb dipole, that is, a pair of strongly deformed counter-rotating vortices, yields results concerning the most unstable wavelengths that are quite close to the present measurements.

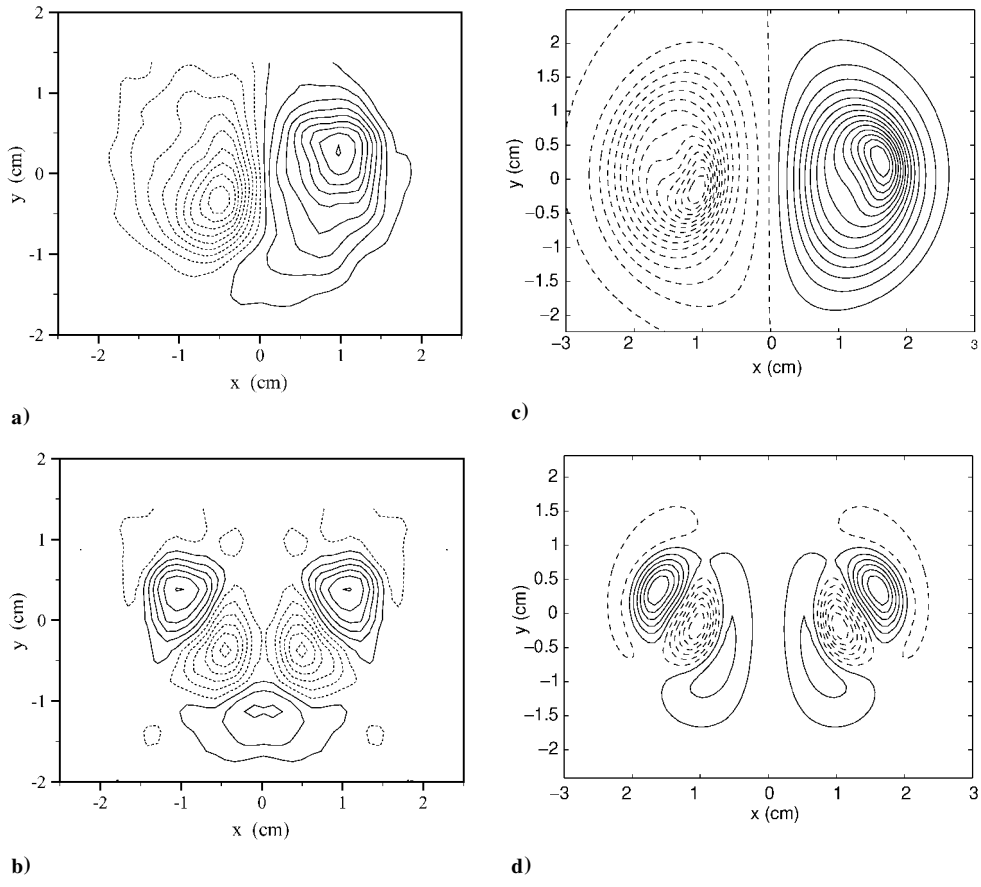

Fig. 5 Axial vorticity in a cross-cut plane: a) experiment, total flow ($Re = 2.4 \times 10^3$, $a/b = 0.2$, and $t^* = 7.5$); b) experiment, perturbation ($Re = 2.4 \times 10^3$, $a/b = 0.2$, and $t^* = 7.5$); c) DNS, total flow ($Re = 2.4 \times 10^3$, $a/b = 0.25$, and $t^* = 12.1$); and d) DNS, perturbation ($Re = 2.4 \times 10^3$, $a/b = 0.25$, and $t^* = 12.1$).

2. Mode Geometry

As shown in Sec. III.A, the perturbation associated with the elliptic instability is characterized by the existence of cylindrical surfaces (tubes), where either the radial perturbation velocity or the perturbation vorticity vanishes. According to theory,[21,23] their diameters d scale on the instability wavelength λ. The invariant streamline tubes have been observed very clearly in the experiments (Fig. 3a), and their diameter was found to be

$$d^S/\lambda = 0.50 \pm 0.03 \qquad \text{(experimental)} \tag{6}$$

which is very close to the theoretical value

$$d^S/\lambda = 0.503 \qquad \text{(theoretical}^{21,23}\text{)} \tag{7}$$

Similarly, the diameter of the invariant tube of axial vorticity was measured in the numerical simulations (see Fig. 3b)

$$d^V/\lambda = 0.67 \pm 0.03 \qquad \text{(numerical)} \tag{8}$$

to be compared to the prediction

$$d^V/\lambda = 0.704 \qquad \text{(theoretical}^{21,23}\text{)} \tag{9}$$

The overall agreement between the present experimental and numerical measurements concerning the geometry of the elliptic instability mode and the corresponding predictions obtained theoretically for a more idealized flow is rather satisfactory.

3. Growth Rates

The growth rate is an important quantity characterizing the instability. It is particularly relevant in the context of aircraft wake vortices, where the desired decay of the initial vortex system is strongly influenced by the growth of instabilities. Figure 7 compares measurements of the time-dependent amplitude of the elliptic instability mode, obtained from experiment and numerical simulation as explained at the beginning of this section. For better comparison, the amplitudes were normalized to be about unity at the start of the growth; no other adjustment was made. Least-squares fits to the linear part of the evolution provide the following nondimensional growth rates:

$$\sigma^* = 0.94 \pm 0.12 \qquad \text{(experimental)} \tag{10}$$

$$\sigma^* = 0.95 \pm 0.30 \qquad \text{(numerical)} \tag{11}$$

The nondimensional growth rate is defined as $\sigma^* = \sigma \times 2\pi b_0^2/\Gamma_0$, σ being the dimensional growth rate. The agreement between the two results, for the growth history in Fig. 7 and the deduced growth rates, is quite remarkable.

A theoretical prediction for the growth rate can be obtained using the results of Eloy and Le Dizès[26] for an inviscid (Gaussian) Lamb–Oseen vortex in a uniform strain field, and the viscous correction term given by Landman and Saffman.[20] The nondimensional theoretical growth rate reads

$$\sigma^* = 1.3790 - (8\pi/Re) \times (ka)_0^2 \big/ (a/b)_0^2 \tag{12}$$

Given a Reynolds number of $Re = 2.5 \times 10^3$ and the average values $(ka)_0 = 1.7$ and $(a/b)_0 = 0.225$ taken from the initial conditions, the most unstable perturbation is predicted to grow with a rate

$$\sigma^* = 0.805 \qquad \text{(theoretical)} \tag{13}$$

that is lower than, but still comparable to, the results found in the present study. This difference is possibly due to the assumption of uniform external strain in the theory, which is maybe too unrealistic in the case of high-(a/b) vortex pairs. Note that the numerical simulations by Billant et al.[24] of a (viscous) Lamb–Chaplygin vortex pair (i.e., a flow resembling more closely the one investigated here

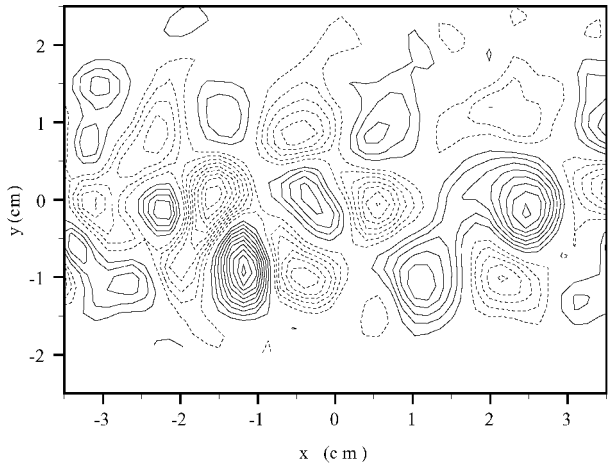

a) Experiment ($Re = 2.4 \times 10^3$, $a/b = 0.2$, and $t^* = 7.5$)

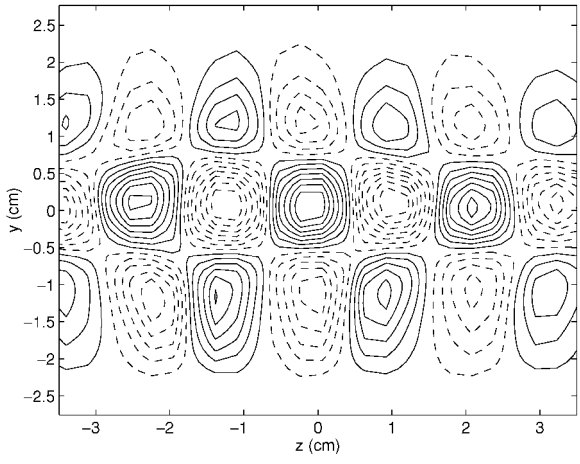

b) DNS ($Re = 2.4 \times 10^3$, $a/b = 0.25$, and $t^* = 12.1$)

Fig. 6 Azimuthal vorticity contours in a vertical plane containing one vortex centerline.

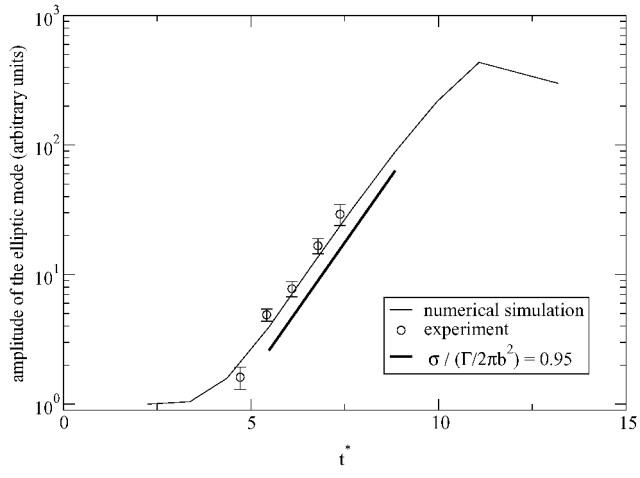

Fig. 7 Growth of the elliptic mode as obtained from experiments (circles) and from the simulation; a reference exponential growth with $\sigma^* = 0.95$ is also plotted.

than the theoretical flow of Refs. 26 and 20) yield a growth rate extremely close to the results in Eqs. (10) and (11).

Note that the inviscid growth rate of the elliptic instability [first term on the right-hand side in Eq. (12)], is almost 40% higher than typical (inviscid) growth rates of the long-wavelength Crow[5] instability.

In summary, the quantitative results that can be extracted from the experiments and numerical simulations concerning the onset and the linear regime of the short-wave vortex pair instability not only show very good agreement between themselves, but both also compare very well to theoretical predictions concerning elliptic instability.

C. Late Stages and Breakdown

As shown in Fig. 7, the growth of the elliptic instability mode is exponential during a certain time interval. In this linear regime, the perturbations are small (compared to the base flow velocities) and take the form described in Sec. III.A. At the end of this regime, the elliptic mode has reached its maximum intensity, and nonlinear interactions with other modes become important. The energy contained in the elliptic mode is redistributed among these other modes, and the amplitude of the basic mode in Fig. 7 is, consequently, found to decrease.

Once the nonlinear regime is reached, the flow experiences a transition to a locally turbulent flow in the following way. As mentioned, the elliptic instability evolves in a cooperative way in the two vortices of the pair due to the large rescaled core size a/b of the present flow. Although the perturbations are coupled in this way, they nevertheless remain mainly located near the vortex centers during the initial linear growth. At large amplitudes, this leads to the configuration in Fig. 5a, where the center of one vortex (the left one in Fig. 5a) is brought close to the stagnation point existing at the lower leading edge of the pair and starts to draw opposite-signed vorticity, which is initially orbiting the other (right) vortex, over to the left side, that is, the vortices now start to interact more intensely. This process is modulated in the axial direction with the wavelength of the instability, so that, actually, tongues of fluid cross over to the other vortex in a periodic interlocking way. The vorticity of these fluid layers, which is originally oriented mainly in the axial direction, is reoriented and stretched by the stagnation point flow at the front of the pair into perpendicular secondary structures, which appear as regularly spaced bridges between the primary axial vortices in Fig. 8. In fact, these bridges consist of counter-rotating vortex pairs. Figure 9 schematically summarizes the formation of these secondary structures; it also shows clearly that two pairs of secondary vortex pairs are generated for each wavelength of the primary deformation.

The secondary azimuthal vortices can be identified clearly in the vertical plane separating the primary vortices. In Fig. 10b, the x component of the vorticity is plotted in this plane. The pattern of opposite-signed vorticity corresponds well to the experimental dye patterns in Fig. 10a. Both show the formation of concentrated vortices through the intensification of this transverse vorticity by the strain at the lower edge of the pair. This interaction via the secondary vortices leads to a strong deformation of the initially rectilinear primary vortices, which is clearly seen in Fig. 11, showing the flow at an advanced stage. The DNS result in Fig. 11b reveals that small-scale structures have been generated from the interaction of primary and secondary vortices, the latter being wrapped around the former after their creation. The mixing and associated generation of small-scale vorticity structures continues in the later evolution of the flow, leading to turbulence, which is almost homogeneous and isotropic in the region of the initial pair, as can be shown by velocity spectra obtained from the numerical simulations. In particular, these results show that the vorticity magnitude, which is initially axial, is redistributed approximately equally into the three spatial directions.[27] The final result is that the initial coherent laminar vortex pair has effectively been destroyed by the strong interaction following the saturation of the elliptic instability.

A different way of illustrating this destruction of the vortex pair is to follow the evolution of the mean circulation of each vortex, the total circulation of the pair always being zero. Figure 12 shows experimental and numerical measurements of the circulation in one half-plane of the flow, for different axial locations, as well as axially averaged. In the experiment, the long-wavelength Crow[5] instability was almost always developing simultaneously, and the result in Fig. 12a represents this mixed case. In the DNS, the initial noise amplitude at the Crow instability wavelength was sufficiently low to yield a pure elliptic instability case. (See also the next section.) Figure 12 shows that the circulation of each vortex starts to decrease

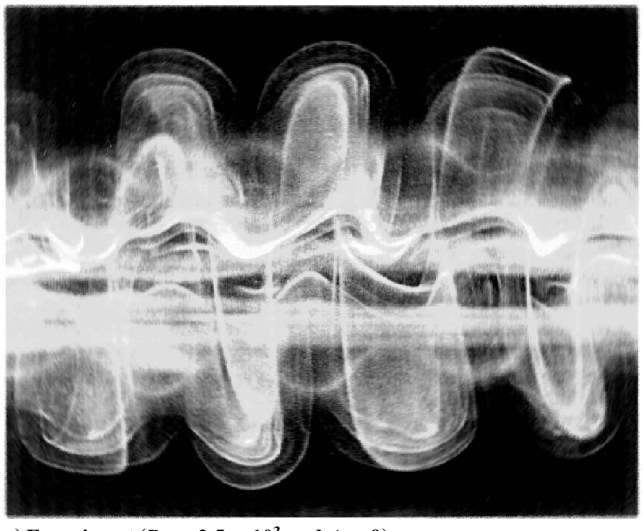

a) Experiment ($Re \approx 2.5 \times 10^3$ and $t^* \approx 9$)

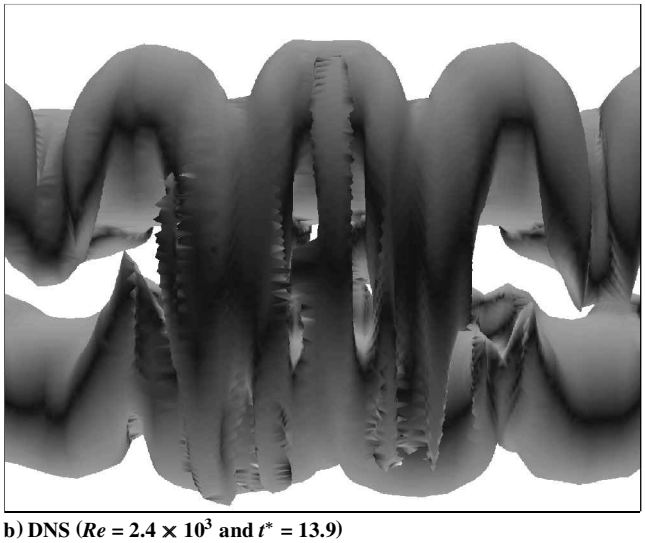

b) DNS ($Re = 2.4 \times 10^3$ and $t^* = 13.9$)

Fig. 8 Creation of secondary transverse vortices.

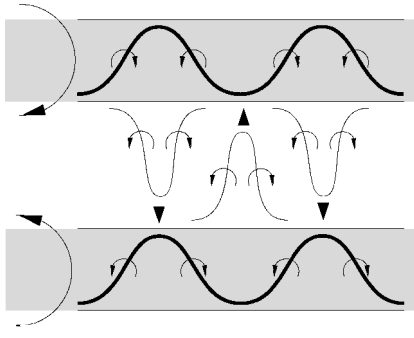

Fig. 9 Schematic top view of the primary vortices deformed by the elliptic mode (bold lines represent the lines of maximal vorticity) and of the creation of the secondary transverse vortex pairs; the sense of rotation (↻) of the primary and secondary vortices, as well as the directions of fluid extraction (►), are given.

a) Experiment ($Re \approx 2.5 \times 10^3$ and $t^* \approx 10$), dye visualization

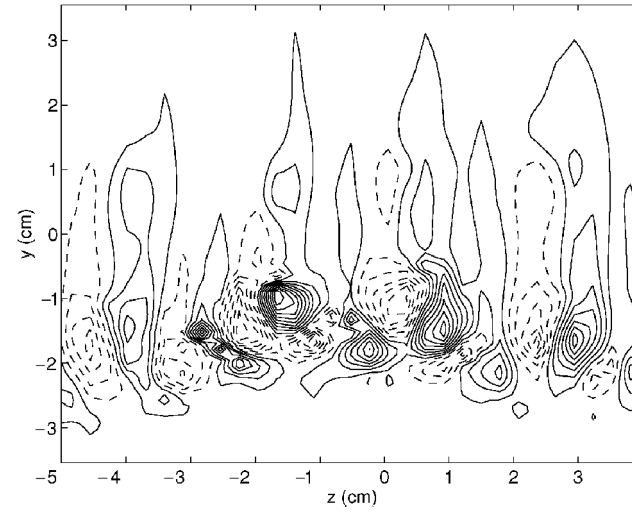

b) DNS ($Re = 2.4 \times 10^3$ and $t^* = 14.8$), contours of ω_x

Fig. 10 Secondary vortices seen in the plane separating the initial vortices.

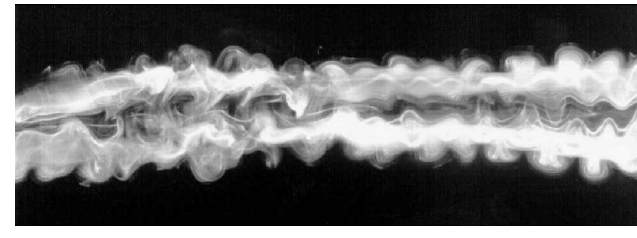

a) Experiment ($Re \approx 2.5 \times 10^3$ and $t^* \approx 8$)

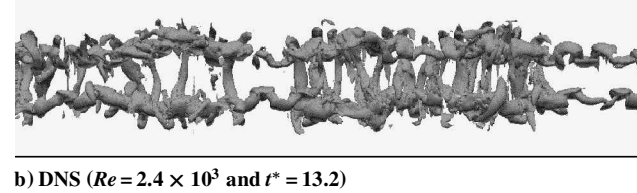

b) DNS ($Re = 2.4 \times 10^3$ and $t^* = 13.2$)

Fig. 11 Advanced stage of the flow after elliptic instability saturation (front view).

quite dramatically, as soon as the strong interaction via the secondary structures sets in. This is due to the enhanced cross diffusion and subsequent annihilation of opposite-signed vorticity from the two sides of the pair. For the pure elliptic instability (Fig. 12b), the circulation drops by about 40%. However, when elliptic and Crow instability develop simultaneously, both experiment and DNS show a decrease of more than 80% of the average circulation, and this takes place over a period of about five nondimensional time units. A phenomenon directly related to this drop in the large-scale circulation is the decrease of the overall descent speed of the pair. Measurements have shown that the pair can slow down by more than 70% with respect to its initial speed.[23]

The results shown in this section show that the final stages of a vortex pair undergoing an elliptic instability are quite different from the case of a pure Crow[5] instability. For the latter, the initial pair ends up as a series of oscillating large-scale vortex rings, and most of the energy and initial circulation is still contained in these structures,

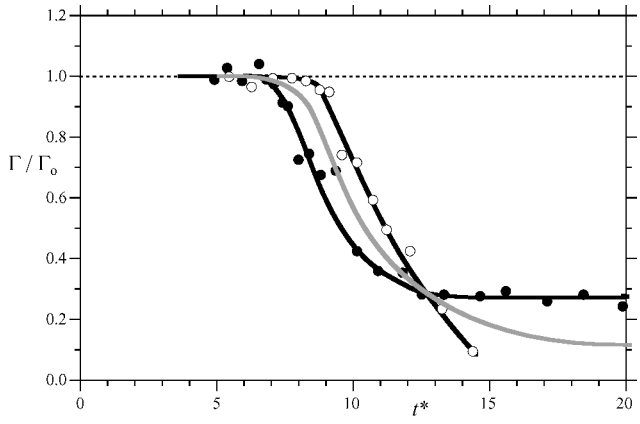

a) Experiment ($Re = 2.66 \times 10^3$)

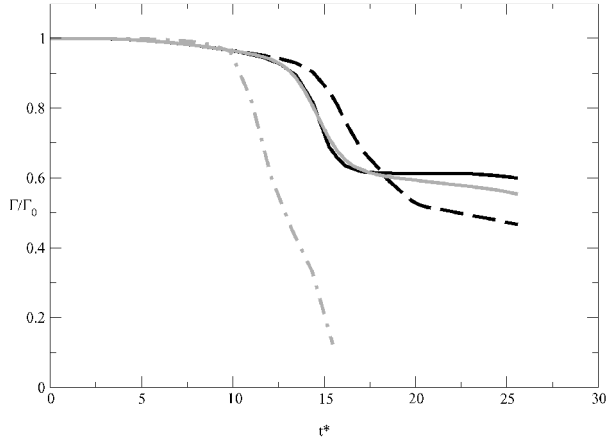

b) DNS ($Re = 2.4 \times 10^3$)

Fig. 12 Evolution of the circulation taken at different axial locations (black) and averaged (gray). Experimental data in a) automatically accounts for the simultaneous development of the Crow[5] and elliptic modes. The numerical results in panel b show the evolution with the elliptic instability alone, as well as a case with both instabilities (dot–dashed curve).

resulting in a practically unchanged descent speed of the system.[10] With the elliptic instability, the counter-rotating vortices are forced into a strong interaction, leading to an effective redistribution of the initial energy into a broad spectrum of small-scale motion, a significant drop in the circulation of each vortex, and a slowing of the vortex pair descent.

IV. Interaction Between Elliptic and Crow[5] Instabilities

A. Context

In the preceding section, we have mainly treated the special case of a pure elliptic instability acting on a laminar vortex pair. However, in a real flow, different modes of instability and, in particular, the long-wavelength Crow[5] instability, may also be growing and enter into competition with the elliptic mode. The amplitudes of these different modes depend mainly on two parameters: their growth rate and their initial amplitude. As mentioned earlier, and further demonstrated in the theoretical work of Widnall et al.[6] and Eloy and Le Dizès,[26] the growth rate of the elliptic instability is larger than the one of the Crow[5] instability for the type of vortex pair flows studied in the present paper ($a/b = 0.2$–0.25). This has also been observed by Billant et al.[24] for the case of a Lamb–Chaplygin vortex pair. Where the initial mode amplitudes are concerned, they depend on the residual background noise present in the flow, or the turbulent motion surrounding the vortex pair in a real atmospheric environment, and, in particular, on the spectral distribution of this noise.

In the experiments described in this paper, the background noise was random and its precise characteristics not known. As a consequence, the observed long-term evolution of the flow was found to vary from one experiment to another, even under otherwise identical conditions (Reynolds number, vortex generator motion, temperature, etc.). Varying relative amplitudes of the elliptic and Crow[5] modes were found, leading to slightly different decay scenarios. In fact, although both instabilities initially develop independently, a certain degree of interaction always appears, in particular during the later stages, as will be illustrated hereafter.

On the other hand, in the numerical study, the initial noise distribution could be very well controlled, and the observed flow evolution could be linked precisely to the initial condition. A useful control parameter for the present case can be defined as the ratio $r = E_{ke}/E_{kc}$, where E_{ke} (E_{kc}) is the initial kinetic energy of the Fourier mode corresponding to the elliptic (Crow[5]) instability. In the numerical simulations, this parameter could be varied by adding, in addition to the white noise, a perturbation consisting of a sinuous deformation of the vortex centerlines, with an axial wavelength matching the most unstable Crow instability mode in the particular flow configuration (given, for example, by Widnall et al.[6]). This additional perturbation was observed to have initially no influence in the range of wavelengths of the elliptic instability.[27] To illustrate the meaning of the parameter r, one may consider the case of homogeneous isotropic turbulence, with an energy distribution given by $E_k \sim k^{-5/3}$. For a wave number ratio $k_e/k_c = 22/3$, which is representative of the experiments and calculations shown in this paper, one finds $r = 3.9 \times 10^{-2}$. The low relative initial energy of the elliptic mode could be one of the reasons for the elliptic instability not being observed clearly in real aircraft trailing vortices so far. (See also discussion in Sec. V.)

B. Possible Evolutions

Variation of the parameter r in the numerical simulations has allowed reproduction of the different long-term evolutions observed in the experiments, thus demonstrating the importance of initial conditions on the development of the vortex pair flow subject to two distinct instabilities. Section III has treated the case of a pure elliptic instability, excited by white noise, for which $r = 1$. (Actually, very similar behavior was observed in the simulations for all $r \geq 5 \times 10^{-2}$.) In the following, two other cases will be discussed: one where both modes appear to be equally important ($r \simeq 9 \times 10^{-3}$) and a second one with a dominant Crow[5] mode ($r \simeq 3.5 \times 10^{-3}$).

Figure 13 presents experimental and numerical visualizations of the flow in these two cases, at an early stage of the interaction between the two instabilities. Both modes are clearly visible, and the development of the two instabilities is only slightly different for the two cases at this time. One common feature is the modulation of the elliptic instability by the Crow[5] mode. An amplification of the former occurs at the locations where the vortices are brought close together by the latter. At these axial positions, the growth rate is found to be larger than in the case of the elliptic instability alone,[27] an increase that can be as large as 45% with respect to the growth rate obtained without Crow[5] instability. At this early stage, the reverse action of the elliptic mode on the Crow instability seems to be weak.

At a later stage, a variety of possible evolutions exists. For large r, the elliptic instability evolves alone, leading to the relatively uniform (in the axial direction) breakdown of the pair shown in Fig. 11. In the opposite case, for vanishing r and dominant Crow[5] instability, the flow evolves toward the well-known formation of periodic vortex rings through a reconnection process, as shown in Figs. 14b and 14d. For intermediate r, the structure of the flow is more complex because at the locations where the Crow mode attempts to reconnect, the elliptic instability is amplified and may lead to a local breakdown. The vortex reconnection is, therefore, more or less significantly perturbed, as can be seen in Fig. 14. In the intermediate case, the rings that are formed just after the instant corresponding to Figs. 14a and 14c are strongly affected by the development of the elliptic mode. They are no longer composed of a single smooth ring, but of many distorted vortical structures that globally form a ringlike structure. This is the case corresponding to the strongest decrease in the average circulation and descent speed discussed in Sec. III.C (Fig. 12). Even in flows with dominant Crow instability (Figs. 14b and 14d), the late stages are modified by the growth of the elliptic

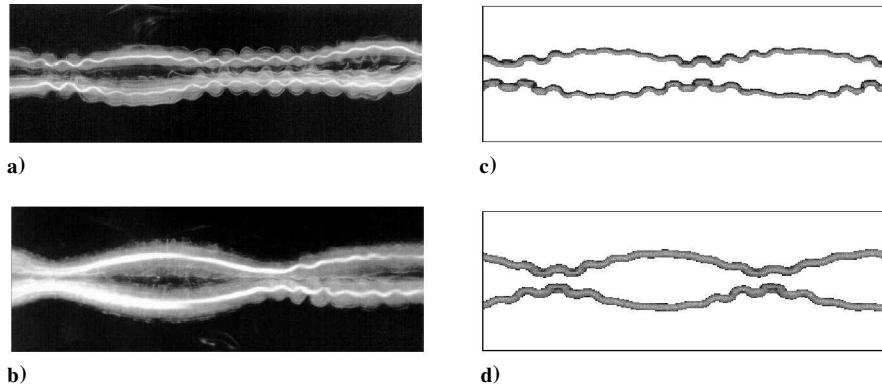

Fig. 13 Early stages of the interaction between elliptic and Crow[5] instabilities: a and c) intermediate case ($r \approx 9 \times 10^{-3}$) and b and d) dominant Crow mode ($r \approx 3.5 \times 10^{-3}$).

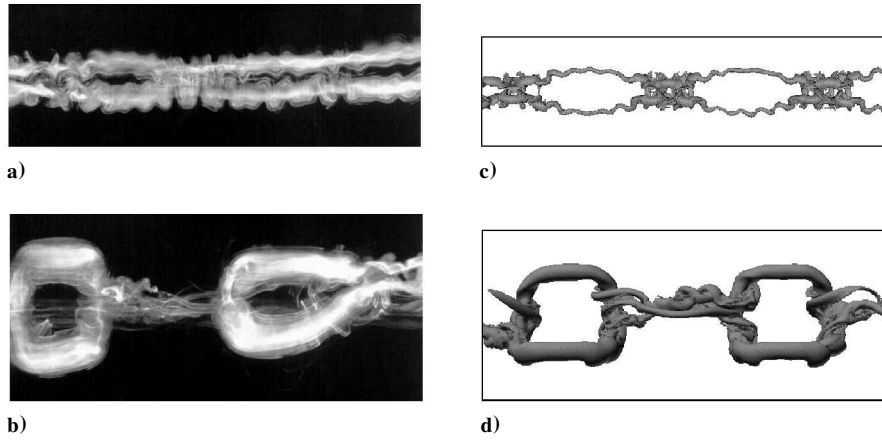

Fig. 14 Late stages of the interaction between both instabilities: a and c) $r \approx 9 \times 10^{-3}$ and b and d) $r \approx 2 \times 10^{-3}$.

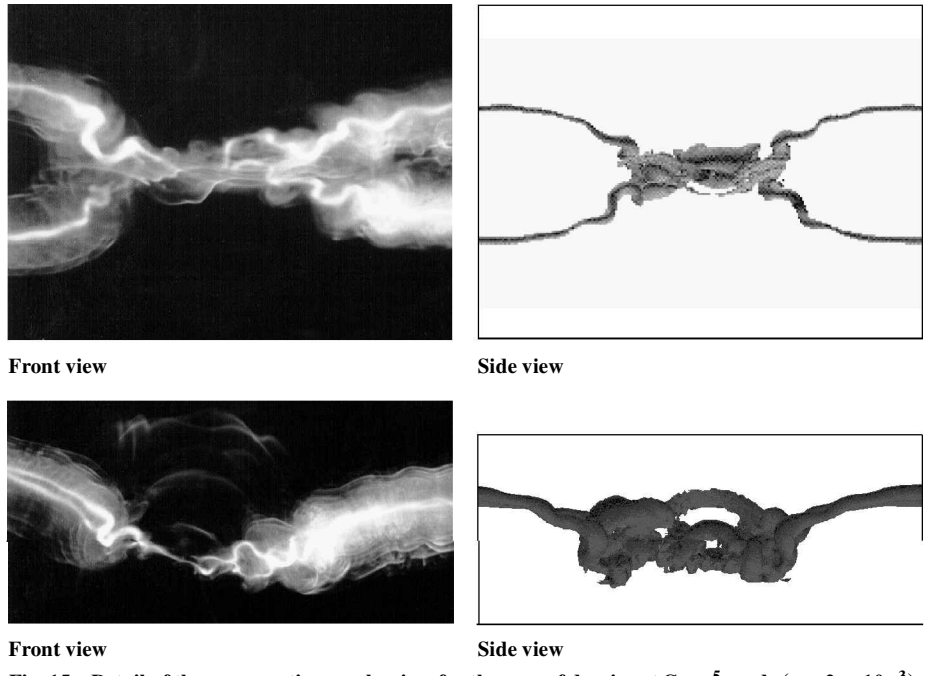

Fig. 15 Detail of the reconnection mechanism for the case of dominant Crow[5] mode ($r \approx 2 \times 10^{-3}$).

mode, resulting in irregular structures between the coherent large-scale vortex rings. Figure 15 shows a close-up visualization of this region from two perpendicular view directions. The wavelength of the elliptic perturbation can clearly be distinguished at both ends of the reconnection region.

The agreement between experimental observations and the results from numerical simulations with different values of the parameter r, characterizing the initial energy distribution, is very good. The results shown in this section demonstrate that the simultaneous development of the short-wavelength elliptic instability and the long-wavelength Crow[5] instability can lead to quite different long-term evolutions of the vortex-pair flow, depending on the spectrum of residual noise or surrounding turbulence present in the flow.

V. Comments on the Relevance to Real Aircraft Wakes

The decay characteristics described in the preceding sections could be of great interest in the context of aircraft wakes, where the principal problem is linked to the long lifespan of the wake

vortices. This problem is of particular importance near airports, specifically concerning aircraft in takeoff and landing phases, in which the aircraft wings are in high-lift configurations, with flaps and slats deployed.

Besides the flow considered here being a simplified model of the flow far downstream of an aircraft, without taking into account effects like external turbulence or stratification, the major differences between the present vortex pairs and real wake vortices concerns the Reynolds number and the nondimensional ratio a/b.

The effect of Reynolds number is expected to be small, influencing mainly the value of the growth rate. This has been confirmed in Ref. 32, where large-eddy simulations with a base flow of similar a/b, but realistic Reynolds numbers of the order of 10^7, were performed. It was also found that, in addition to the larger growth rates obtained in these simulations, the dynamics remained similar to the low Reynolds number experiments and simulations. In particular, the same transition mechanisms have been found to occur at these large Reynolds numbers.

In the present study, we consider flows with $a/b \approx 0.2$–0.25, whereas this ratio is of the order of $a/b \approx 0.05$ for real wakes downstream of an aircraft in high-lift configuration.[33] (This value has been obtained for an aircraft equipped with a single flap, for which each vortex of the counter-rotating pair remaining in the far-field results from the merging of the wing tip and the outboard flap vortices.) This large difference in the ratio a/b implies a much larger difference in the wavelengths of the elliptic instability (scaling on a) and the Crow[5] instability (scaling on b). On the one hand, if one considers an atmospheric environment of approximately homogeneous isotropic turbulence, this scale separation results in an energy distribution that is even less favorable for the development of the elliptic instability than for the present flow, as discussed at the end of Sec. IV.A. On the other hand, in a recent weakly nonlinear analysis of such flows, Sipp[34] has shown that low a/b would lead to alternating cycles of increase and decrease, with only a small maximum amplitude of the elliptic mode and no breakdown. However, Kerswell[35] had shown earlier that, even for small amplitudes, the elliptic mode can undergo secondary instabilities by exciting the growth of other normally neutral inertial-wave (or Kelvin) modes of the vortex, modes that were excluded from the start in Sipp's[34] study. These secondary instabilities, and further nonlinear interactions between more and more modes could then possibly still lead to a breakdown of the flow into small-scale turbulence. The characteristic timescale for this breakdown is nevertheless expected to be quite long, and other decay mechanisms, such as decay induced by atmospheric turbulence, would most likely dominate this process.

Other important differences, e.g., vorticity profiles different from Gaussian distributions or the presence of axial flow in the vortex cores in real aircraft trailing wakes, may have a significant influence on the development of the elliptic instability.

From these arguments, it is not surprising that, to the authors' knowledge, the elliptic instability has not been observed in real aircraft wakes because the conditions, in particular concerning the rescaled core size, are too far from the ones in the present study. In a recent paper by Rossow and James,[36] the presence of circumferential striations corresponding to eddies aligned around the outside of the wake condensation cloud was observed. These eddies are formed early in the wake history. Such eddies are also formed in the flow considered here during and after the transition regime; they result from the transverse vortices that lead to the complete decay of the primary vortex pair (Fig. 8). Even if the scales and circumstances of the present flow are quite different from the ones in aircraft wakes, it was argued by Rossow and James that the observed eddies could be a result of the elliptic instability. Because of the much smaller a/b in aircraft wakes, this seems to be quite unlikely, as discussed earlier. The observed eddies are believed to be formed by the action of the counter-rotating vortex pair on the external surrounding turbulence. As discussed in Ref. 27, the late stages of the elliptic instability are similar to the evolution of a vortex pair in a turbulent atmosphere, including the existence of transverse vortices. The numerical studies of Risso et al.[37] and Moet et al.[38] describe in detail the mechanism of eddy formation along the streamlines of the vortex pair flow in the vicinity of the hyperbolic stagnation points.

Despite all of this, it seems quite obvious that the interaction between real aircraft wake vortices leading to the rapid decay described in Sec. III.C may occur if the relative core size a/b can be increased in the far field to a value of the order of 0.2. Efforts could be directed toward such an increase, for example, by redistributing the wing load of a given aircraft to diminish the vortex spacing, and/or by increasing the vortex core radius by active or passive methods. Counter-rotating vortices with large relative core sizes exist already behind aircraft equipped with split flaps. In such configurations, opposite-signed vortices with potentially different vortex radii and circulations are shed by the inboard and outboard flap edges. The present results may be relevant to such existing situations.

VI. Summary

We have presented a direct comparison between results from an experimental study and DNS calculations of a laminar pair of closely spaced counter-rotating vortices at low Reynolds number undergoing the short-wavelength elliptic instability. Excellent qualitative and quantitative agreement was found concerning the initial stages of the instability (spatial structure of the unstable mode, wavelengths, and growth rates), as well as the different types of long-term evolution, depending on different degrees of interaction with the long-wavelength Crow[5] instability that is also present in this type of flow. The parameter governing this interaction has also been clearly identified; it involves the initial energy distribution among the different wavelengths.

A remarkable feature of the nonlinear regime of the elliptic instability is that it causes a strong exchange between the two initial vortices through the formation of perpendicular secondary vortex pairs. This leads to a sudden breakdown of the flow into small-scale turbulent motion, accompanied by a sharp drop in the circulation of each initial vortex due to the enhanced cross diffusion of vorticity and a significant decrease in the vortex pair descent speed. These effects are found to be even stronger when the elliptic instability interacts with a simultaneously developing Crow[5] instability, a feature that could be relevant for the problem of aircraft trailing wakes.

Acknowledgments

The experiments were performed in the Fluid Dynamics Research Laboratory of Charles Williamson at Cornell University. The computational work was carried out under the direction of Alexandre Corjon at the European Center for Research and Advanced Training in Scientific Computation in Toulouse, France. We express our gratitude to both for the opportunity to carry out this work and for invaluable support.

References

[1] *The Characterization and Modification of Wakes from Lifting Vehicles in Fluids*, Vol. 584, CP, AGARD, 1996.

[2] Spalart, P. R., "Airplane Trailing Vortices," *Annual Review of Fluid Mechanics*, Vol. 30, 1998, pp. 107–138.

[3] Rossow, V. J., "Lift-Generated Vortex Wakes of Subsonic Transport Aircraft," *Progress in Aerospace Sciences*, Vol. 35, No. 6, 1999, pp. 507–660.

[4] Gerz, T., Holzäpfel, F., and Darracq, D., "Commercial Aircraft Wake Vortices," *Progress in Aerospace Sciences*, Vol. 38, No. 3, 2002, pp. 181–208.

[5] Crow, S. C., "Stability Theory for a Pair of Trailing Vortices," *AIAA Journal*, Vol. 8, No. 12, 1970, pp. 2172–2179.

[6] Widnall, S. E., Bliss, D., and Zalay, A., "Theoretical and Experimental Study of the Stability of a Vortex Pair," *Aircraft Wake Turbulence and Its Detection*, edited by J. H. Olsen, A. Goldberg, and M. Rogers, Plenum, New York, 1971, pp. 305–338.

[7] Eliason, B. G., Gartshore, I. S., and Parkinson, G. V., "Wind Tunnel Investigation of Crow Instability," *Journal of Aircraft*, Vol. 12, No. 12, 1975, pp. 985–988.

[8] Sarpkaya, T., "Trailing Vortices in Homogeneous and Density-Stratified Media," *Journal of Fluid Mechanics*, Vol. 136, 1983, pp. 85–109.

[9] Liu, H.-T., "Effects of Ambient Turbulence on the Decay of a Trailing Vortex Wake," *Journal of Aircraft*, Vol. 29, No. 2, 1992, pp. 255–263.

[10] Leweke, T., and Williamson, C. H. K., "Long-Wavelength Instability and Reconnection of a Vortex Pair," *IUTAM Symposium on Dynamics of Slender Vortices*, edited by E. Krause and K. Gersten, Kluwer Academic Publishers, Dordrecht, The Netherlands, 1998, pp. 225–234.

[11] Scorer, R. S., and Davenport, L. J., "Contrails and Aircraft Downwash," *Journal of Fluid Mechanics*, Vol. 43, 1970, pp. 451–464.

[12]Tombach, I., "Observations of Atmospheric Effects on Vortex Wake Behavior," *Journal of Aircraft*, Vol. 10, No. 11, 1973, pp. 641–647.

[13]Chevalier, H., "Flight Test Studies of the Formation and Dissipation of Trailing Vortices," *Journal of Aircraft*, Vol. 10, No. 1, 1973, pp. 14–18.

[14]Widnall, S. E., Bliss, D., and Tsai, C.-Y., "The Instability of Short Waves on a Vortex Ring," *Journal of Fluid Mechanics*, Vol. 66, 1974, pp. 35–47.

[15]Moore, D. W., and Saffman, P. G., "The Instability of a Straight Vortex Filament in a Strain Field," *Proceedings of the Royal Society London A*, Vol. 346, No. 1646, 1975, pp. 413–425.

[16]Tsai, C.-Y., and Widnall, S. E., "The Stability of Short Waves on a Straight Vortex Filament in a Weak Externally Imposed Strain Field," *Journal of Fluid Mechanics*, Vol. 73, 1976, pp. 721–733.

[17]Robinson, A. C., and Saffman, P. G., "Three-Dimensional Stability of an Elliptical Vortex in a Straining Field," *Journal of Fluid Mechanics*, Vol. 142, 1984, pp. 451–466.

[18]Pierrehumbert, R. T., "Universal Short-Wave Instability of Two-Dimensional Eddies in an Inviscid Fluid," *Physical Review Letters*, Vol. 57, No. 17, 1986, pp. 2157–2159.

[19]Bayly, B. J., "Three-Dimensional Instability of Elliptical Flow," *Physical Review Letters*, Vol. 57, No. 17, 1986, pp. 2160–2163.

[20]Landman, M. J., and Saffman, P. G., "The Three-Dimensional Instability of Strained Vortices in a Viscous Fluid," *Physics of Fluids*, Vol. 30, No. 8, 1987, pp. 2339–2342.

[21]Waleffe, F., "On the Three-Dimensional Instability of Strained Vortices," *Physics of Fluids A*, Vol. 2, No. 1, 1990, pp. 76–80.

[22]Lifschitz, A., and Hameiri, E., "Local Stability Conditions in Fluid Dynamics," *Physics of Fluids A*, Vol. 3, No. 11, 1991, pp. 2644–2651.

[23]Leweke, T., and Williamson, C. H. K., "Cooperative Elliptic Instability of a Vortex Pair," *Journal of Fluid Mechanics*, Vol. 360, 1998, pp. 85–119.

[24]Billant, P., Brancher, P., and Chomaz, J.-M., "Three-Dimensional Stability of a Vortex Pair," *Physics of Fluids*, Vol. 11, No. 8, 1999, pp. 2069–2077.

[25]Kerswell, R. R., "Elliptical Instability," *Annual Review of Fluid Mechanics*, Vol. 34, 2002, pp. 83–113.

[26]Eloy, C., and Le Dizès, S., "Three-Dimensional Instability of Burgers and Lamb–Oseen Vortices in a Strain Field," *Journal of Fluid Mechanics*, Vol. 378, 1999, pp. 145–166.

[27]Laporte, F., and Corjon, A., "Direct Numerical Simulations of the Elliptic Instability of a Vortex Pair," *Physics of Fluids*, Vol. 12, No. 5, 2000, pp. 1016–1031.

[28]Locke, C. A., Hirsa, A., and Rubin, M. D., "Short-Wave Instability in a Laminar Vortex Pair," *ASME Fluids Engineering Conference, Forum on Unsteady Flows*, edited by W. L. Keith and T. Wei, Vol. 157 of FED, American Society of Mechanical Engineers, New York, 1993, pp. 73–81.

[29]Thomas, P. J., and Auerbach, D., "The Observation of the Simultaneous Development of a Long and a Short-Wave Instability Mode on a Vortex Pair," *Journal of Fluid Mechanics*, Vol. 256, 1994, pp. 289–302.

[30]Orlandi, P., Carnevale, G. F., Lele, S. K., and Shariff, K., "DNS Study of Stability of Trailing Vortices," *Proceedings of the Summer Program 1998*, edited by P. Moin and W. C. Reynolds, Center for Turbulence Research, Stanford Univ., Stanford, CA, 1998, pp. 187–208.

[31]Lele, S. K., "Compact Finite Difference Schemes with Spectral-Like Resolution," *Journal of Computational Physics*, Vol. 103, No. 1, 1992, pp. 16–42.

[32]Laporte, F., "Simulation Numérique Appliquée à la Caractérisation et aux Instabilités des Tourbillons de Sillage d'Avions de Transport," Ph.D. Dissertation, Institut National Polytechnique/CERFACS, Toulouse, France, 2002.

[33]Jacquin, L., Fabre, D., Geffroy, P., and Coustols, E., "The Properties of a Transport Aircraft Wake in the Extended Near Field: An Experimental Study," AIAA Paper 2001-1038, 2001.

[34]Sipp, D., "Weakly Nonlinear Saturation of Short-Wave Instabilities in a Strained Lamb–Oseen Vortex," *Physics of Fluids*, Vol. 12, No. 7, 2000, pp. 1715–1729.

[35]Kerswell, R. R., "Secondary Instabilities in Rapidly Rotating Fluids: Inertial Wave Breakdown," *Journal of Fluid Mechanics*, Vol. 382, 1999, pp. 283–306.

[36]Rossow, V. J., and James, K. D., "Overview of Wake-Vortex Hazards During Cruise," *AIAA Journal*, Vol. 37, No. 6, 2000, pp. 960–975.

[37]Risso, F., Corjon, A., and Stoessel, A., "Direct Numerical Simulations of Wake Vortices in Intense Homogeneous Turbulence," *AIAA Journal*, Vol. 35, No. 6, 1997, pp. 1030–1040.

[38]Moet, H., Darracq, D., Laporte, F., and Corjon, A., "Investigation of Ambient Turbulence Effects on Vortex Evolution Using Large-Eddy Simulation," AIAA Paper 2000-0756, 2000.

H. M. Atassi
Associate Editor